Journal of Quantitative Spectroscopy & Radiative Transfer 346 (2025) 109598

Contents lists available at ScienceDirect

Journal of Quantitative Spectroscopy and Radiative Transfer

journal homepage: www.elsevier.com/locate/jqsrt

Simultaneous hyperspectral imaging and pyrometry for multi-phase temperature profiling of energetic composite reactions

Qinghui Meng [a], Erik Hagen [b], Colin Goodman [c], Mark A. Foster [c], Michael R. Zachariah [a,*]

[a] *Department of Chemical and Environmental Engineering, University of California, Riverside, CA 92521, United States*
[b] *Materials Science and Engineering, University of California, Riverside, CA 92521, United States*
[c] *Department of Electrical and Computer Engineering, Johns Hopkins University, MD 21218, United States*

ARTICLE INFO

Keywords:
2D multi-phase temperature measurements
Hyperspectral emission spectroscopy
Energetic composites
High-speed imaging

ABSTRACT

High-temperature, multi-phase reactions in energetic composites present significant challenges in understanding their chemical processes and underlying mechanisms. These systems often involve rapid, heterogeneous reactions which require temporally and spatially resolved diagnostic tools. To address this need, this work develops a dual-camera system that integrates hyperspectral emission spectroscopy and three-color pyrometry, enabling simultaneous, high-speed measurements of gas-phase and condensed-phase temperatures. One camera captures RGB video for three-color pyrometry, while the other captures emission spectra using a slit-array mask and diffraction grating system. The slit-array mask is designed to achieve spatial coverage, allowing for 2D gas-phase temperature profiling. Gas-phase temperatures are derived using emission spectra based on Boltzmann equation, utilizing the intensity ratios of potassium emission lines near 580 nm and 693 nm. Demonstration experiments were conducted using 3D-printed Al-$KClO_4$ thermites with varying equivalence ratios, revealing maximum gas-phase temperatures of 3300–3700 K, and condensed-phase temperatures about 2800 K. The gas-phase temperatures closely align with the material's adiabatic flame temperatures, and the condensed phase temperatures of aluminum droplets are close to aluminum boiling point (2743 K). This diagnostic system offers significant advancements in the study of energetic materials by enabling synchronous, high-speed measurements of gas-phase and condensed-phase temperature distributions. Its capability for 2D profiling and adaptability to other high-temperature reaction systems represents a critical step forward in advancing fundamental research on energetic materials and combustion. The outcome of this work lays the foundation for exploring thermal dynamics and chemical kinetics in energetic composites, facilitating the design of nanostructured energetic materials.

1. Introduction

Energetic composites – mixtures of high energy density metals (e.g. Al, Ti, B, Mg) and oxidizers (e.g. $KClO_4$, CuO, Fe_2O_3) – are of interest in various applications requiring rapid and controlled release of vast amounts of energy, such as pyrotechnics, cutting and welding, construction and mining, defense, and aerospace systems [1–3]. Recent advancements in the design of energetic composites, such as additive manufacturing of energetic materials [4–6], particle surface treatment [7,8], nanostructure design [1,6,9], and tailored composite formulations [10], have considerably enhanced their performance. The complexity of these designed energetic composite reactions cannot be overestimated, which involve rapid heat release, multi-phase interactions, and complex heat and mass transfer processes. This poses significant diagnostic challenges in evaluating and revealing the underlying reaction mechanisms.

The destructive nature of energetic material reactions limits the applicability of conventional contact-based measurements, such as thermocouples, which suffer from poor spatial and temporal resolution and can fail in high-temperature environments. Optical spectroscopy diagnostic methods, such as laser absorption spectroscopy [11,12] and Coherent Anti-Stokes Raman Spectroscopy (CARS) [13,14], have high temporal resolution, but also face limitations when applied to energetic material reactions due to interference and obstruction from the condensed phase produced during these reactions.

High-speed imaging methods offer the advantages of high temporal and spatial resolution, which are invaluable in resolving the heterogenous reacting phenomenon of energetic composites [15,16]. For

---

* Corresponding author.
E-mail address: mrz@engr.ucr.edu (M.R. Zachariah).

https://doi.org/10.1016/j.jqsrt.2025.109598
Received 28 March 2025; Received in revised form 16 July 2025; Accepted 23 July 2025

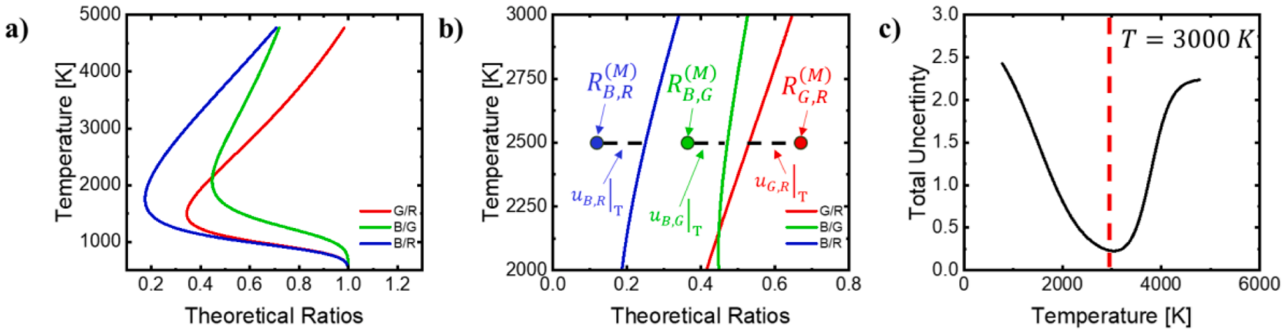

Fig. 1. a) Temperatures and the corresponding theoretical ratios. Note the inflection point. b) Zoomed in of (a) and depicts an example of a single uncertainty calculation for $T = 3000$ K. The colored dots correspond to a corrected, measured ratio and the black line represents $u_{i,j}|_{T\,=\,3000K}$ for each measured value. c) An example of the total uncertainty of a single pixel over the range of temperatures available. In this case the minimum uncertainty is approximately $T = 3000$ K.

instance, three-color pyrometry enables the determination of condensed-phase temperatures from images captured by high-speed RGB cameras. However, because RGB cameras capture signals as integrated wavelength ranges for each R, G, B channel, they cannot resolve detailed spectral features and are easily affected by light emissions from species. Other imaging techniques, such as holography, X-ray contrast imaging and Schlieren methods, provide larger depths of field, making them useful for tracking particles trajectories and observing condensed-phase reacting surface, but do not provide any spectral information [17–19].

Snapshot hyperspectral imaging has gained attention across a variety of fields for its ability to resolve the detailed spectral information in both spatial and temporal domains [20–22]. For energetic material diagnostics, it offers new opportunities by combining spectral analysis with high-speed imaging. This combination enables the capture of additional data, such as blackbody radiation, emission spectra, and fluorescence signals, which can be used to determine species distribution and temperatures.

Most of the previously developed methods for observing energetic materials reactions focus on measuring single phase properties. For heterogeneous combustion, enabling simultaneous measurement of both the condensed phase and gas phase provides more opportunities to understand the reaction, heat transfer, and mass transfer mechanism in both phases. With this goal, this work develops a dual-camera high-speed imaging system that simultaneously provides 2D spatially resolved spectroscopy and pyrometry data, with demonstrations showing transient reactions of Al-$KClO_4$ thermites. An RGB camera captures direct observations of the reaction front during thermites combustion, and offers condensed-phase temperature measurements through three-color pyrometry [15]. A monochrome camera captures the light sampled by a slit-mask and dispersed by a diffraction grating, providing measurements of potassium emission peaks, from which the gas phase temperatures are determined. This system addresses the challenge of resolving temperature profiles in energetic composite reactions, advancing the fundamental understanding of combustion dynamics and facilitating the design of next-generation energetic materials. Beyond the energetic composite reactions examined in this work, the proposed method has potential applications in a wide range of high-temperature, transient reacting systems.

2. Methodology

2.1. Theoretical background

2.1.1. Three-color pyrometry imaging for condensed-phase temperature measurements

A comprehensive overview and in-depth discussion regarding multi-spectral pyrometry can be found in [23]. The three-color pyrometry imaging method used in this study is based on our previous work [24]. In summary, three-color pyrometry uses signals from the R, G, B channels of a camera and the Planck's gray body emission law (Eq. (1)) to measure temperatures.

$$B(\lambda, T) = \frac{2hc^2}{\lambda^5} \times \epsilon\left(\exp\left(\frac{hc}{\lambda k_B T}\right) - 1\right)^{-1} \tag{1}$$

where h, c, and k_B, represent Planck's constant, the speed of light, and Boltzmann's constant respectively, while λ is the wavelength. It is assumed that the gas is optically thin, and the emissivity (ε) remains constant across different wavelengths. This assumption has been commonly adopted in previous studies that used pyrometry to measure the temperature of aluminum combustion [17,24,25] and explosives [26]. Some studies have reported wavelength-dependent emissivity for nano-scale alumina particles [27–29]. However, such effects are not directly relevant to the current work, which focuses on micrometer-scale liquid aluminum droplets at the reaction front. Thus, the radiance B is only determined by λ and T.

The signal captured by the RGB camera represent integrated radiance of the three channels. For a given temperature T, theoretical intensity ratios can be calculated using Eq. (2):

$$R_{i,j}^{(Theory)} = \frac{\int B(\lambda, T)\alpha_i(\lambda)d\lambda}{\int B(\lambda, T)\alpha_j(\lambda)d\lambda} \tag{2}$$

where subscripts i and j refer to different channels, α(λ) is the spectral response curve for a single channel. α(λ) and the modified response curve considering the 594 nm notch filter are provided in supplementary materials (Figure S2).

Fig. 1(a) shows $R_{i,j}^{(Theory)}$ for the channel combinations, where all curves exhibit inflection points within the 1500–2000 K temperature range. Consequently, polynomial fitting is not a viable option for directly determining temperatures from the measured ratios (i.e., one measured ratio gives two temperatures). Instead, a brute-force minimization method is employed. For each camera pixel, the measured G/R, B/R and B/G ratios are first corrected using calibration factors. A blackbody source (Thorlabs Tungsten-Halogen Light Source, SLS201L) is used to determine the calibration factors, with details provided in supplementary materials. Then, for temperatures ranging from 773 K to 4773 K in 1 K steps, the differences between the theoretical ratios at each temperature and the corrected measured ratios are computed. The goal is to determine the temperature at which the total uncertainty U_T is minimized, defined as the sum of the deviations between the corrected measured ratios and the theoretical ratios, as shown in Eq. (3). An example of the determination process of U_T is shown in Fig. 1 (b-c).

$$\begin{aligned} U_T &= \min\left(u_{G,R}\big|_T + u_{B,R}\big|_T + u_{B,G}\big|_T\right) \\ u_{i,j}\big|_T &= \left|R_{i,j}^{(Measured)} - R_{i,j}^{(Theory)}\right|_T, \ i,j = R,\ G,\ B \end{aligned} \tag{3}$$

The determined lowest U_T and the corresponding temperature are

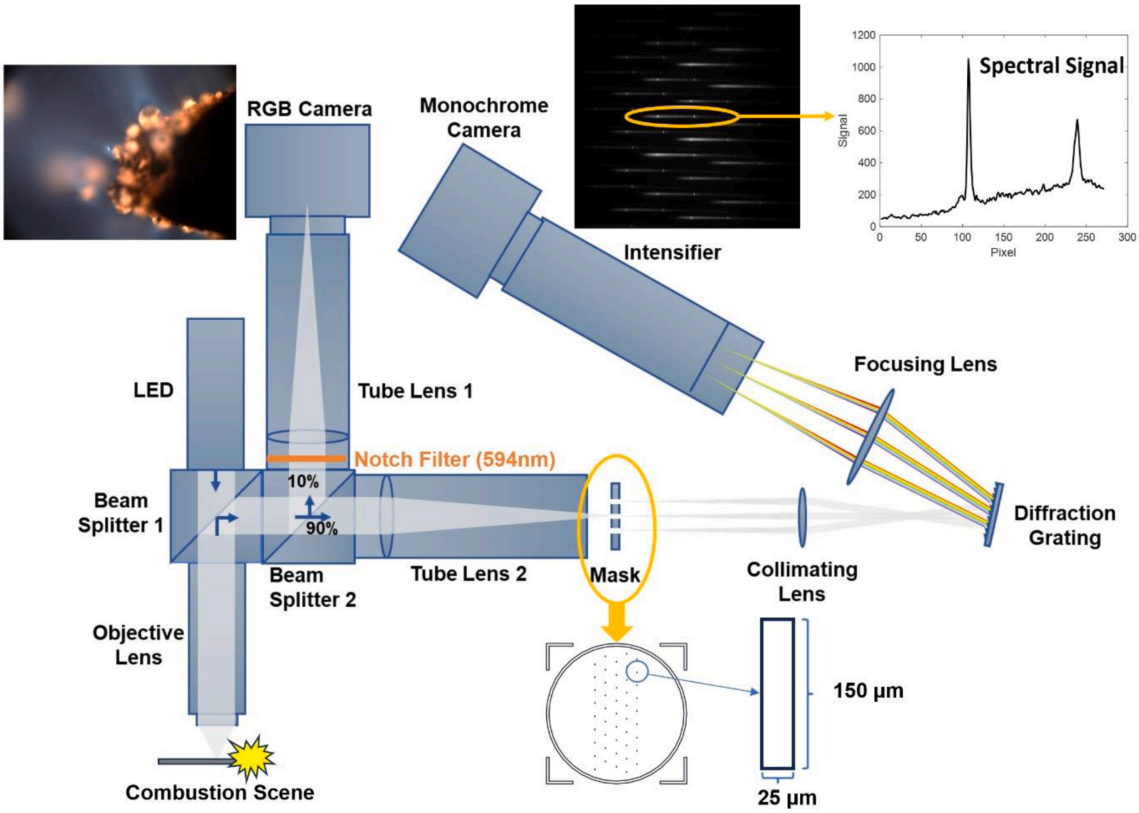

Fig. 2. Experimental setup of the dual-camera spectroscopy and pyrometry design. The emitted light from the combustion scene is represented by the gray shadows. Examples of the images captured by both cameras are displayed next to the camera symbols.

assigned to each pixel. Temperatures with high U_T (above a threshold of 0.2) are filtered out. Additionally, pixels with saturation or low absolute intensity, which do not provide reliable measurements, are also removed. A low-intensity threshold of 15 % of the maximum intensity is applied.

2.1.2. Emission spectroscopy for gas-phase temperature measurement

The spectroscopy arm of this system is designed to capture the spatially resolved emission spectrum, with the primary goal of obtaining the spatially resolved gas-phase temperature at high frame rate. Atomic emission spectroscopy is a well-established method for temperature measurement in flames, and its detailed theoretical foundations can be found in [30]. For clarity, a brief introduction along with the most relevant equations is provided here to support the data analysis procedures discussed in Section 2.4.

In high temperature environments such as flames and plasmas, atoms can emit light at characteristic wavelengths as they transition from excited states to lower energy states [31]. The intensity of these emissions depends on both temperature and species concentration, as described by the Boltzmann equation:

$$I_{\lambda i} = kN^{*}{}_{\lambda i} = kN\cdot\left(\frac{g_{\lambda i}}{g_0}\right)\cdot e^{-\frac{E_{\lambda i}}{k_B T}} \tag{4}$$

where I is the emission light intensity at excited state i with wavelength λ_i, k is a constant accounting for the transition efficiency, N^* is the number of atoms in the excited state i, N is the total number of atoms, g_i and g_0 are statistical weights of the excited state i and the ground state respectively, E_i is the relative energy of the excited state i, and k_B is Boltzmann's constant (1.38×10^{-23} J/K), T is the temperature in K. g_i, g_0 and E_i values can be obtained from NIST Atomic Spectra Database [32] and also provided in Supplementary Materials (Table S1). Note that, selection of database may cause a systematic error of the derived temperatures from ratios, which however, does not affect the temperature trends. A comparison of temperature-ratio curves from different databases is provided in the Supplementary Materials (Figure S4).

To derive the temperature from the emission spectrum, at least two emission lines are required to eliminate unknown factors such as k and N. Using the intensities of two emission lines, the temperature can be determined by the following equation, where 1 and 2 represents two distinct emission states with different wavelength:

$$T = \frac{E_{\lambda 2} - E_{\lambda 1}}{k_B \ln\left(\frac{I_{\lambda 1} g_{\lambda 2}}{I_{\lambda 2} g_{\lambda 1}}\right)} \tag{5}$$

However, not all emission lines are suitable for temperature determination. Several criteria must be met. First, the selected element must exhibit strong atomic emission under the experimental temperature range. For flame studies, where typical temperatures are below 4000 K, alkali metals are ideal because of their strong emission lines in this range. In addition, the chosen spectral lines must have a ratio sensitive to temperature variations while remaining within the detector's dynamic range. This ensures accurate capture of both line intensities by the spectrometer.

Evaluation results for alkali metals, including K, Na, Ca, Cs and Li, are provided in the supplementary materials (Figure S5). These results indicate that the potassium emission lines near 580 nm and 694 nm are optimal for temperature measurements in the range of 2000–4000 K.

2.2. Experimental setup

The dual-camera imaging system, shown in Fig. 2, consists of two optical arms for pyrometry imaging (condensed phase temperature) and hyperspectral imaging (gas phase temperature). A photo of the setup is provided in the supplementary materials (Figure S1). A white LED light source (ASI MIM-LED-LAMP) on the left side of the setup was used to

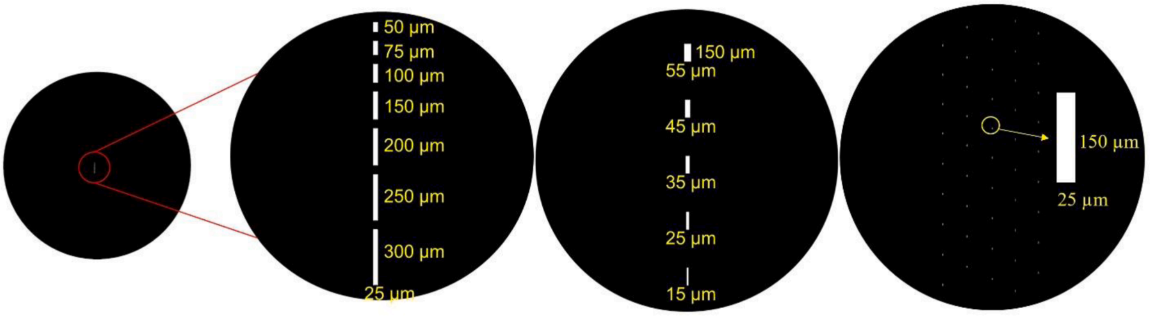

Mask A/B Mask A (Enlarged) Mask B (Enlarged) Mask C

Fig. 3. Slit designs on different masks. Mask A have slits with fixed width at 25 μm and various heights of 50 – 300 μm. Mask B have slits with fixed height at 150 μm and various widths of 15 – 55 μm. Mask A and B are designed for SNR analysis. Mask C has 2D distributed slits with width at 25 μm and height at 150 μm, designed for spatial K emission spectra measurements.

align the sample with the focal plane of the objective lens prior to experiments. Light emitted by the thermite reactions was collected by an objective lens (Mitutoyo 10X Plan Apo) and split by two beam splitters. 10 % of the light at the second beam splitter was directed to an RGB camera (Phantom VEO1310) for pyrometry imaging, while the remaining 90 % was directed to the spectroscopy arm. A notch filter (Thorlabs NF594–23) was attached behind the beam splitter and before tube lens 1, in order to remove Na emissions impact on pyrometry measurement. Using the Bayer filter, the RGB camera enables three-color pyrometry imaging and is based on our prior work [24]. The spatial resolution for the RGB camera is 1.756 μm/pixel.

The purpose of the spectroscopy arm is to collect spatially resolved atomic or diatomic emission spectra. For the demonstration in this work, the purpose is to extract local gas phase temperatures, which can then be simultaneously overlayed with the condensed phase temperatures. To do this, a slit-mask was placed at the focal plane of tube lens 2 to enable only selected regions of the imaged scene to have dispersed light imaged on the monochrome camera. The slit design, further described in Section 2.3, allowed spatially resolved measurements. Light passing through the slits, is collimated by a lens ($f = 150$ mm) and directed to a plane-ruled diffraction grating (150 grooves/mm, Newport). The focal length and grove density were selected to ensure that the spatially distributed spectra fit within the monochrome camera detector while providing sufficient spectral resolution to resolve the emission peaks. The first-order diffracted light was captured by an intensifier (Lambert Instruments, HiCATT25) to intensify the signal, then captured by a high-speed monochrome camera (Phantom VEO1310S) for gas phase temperature analysis. Details on camera calibration and data processing methods are provided in Section 2.4. Raw images of the reaction scene captured by the two cameras are shown next to the cameras.

2.3. Mask design considerations

The position and shape of the slits on the mask are critical, as they directly influence the spatial resolution, signal-to-noise ratios (SNR), and the width of emission peaks. Intuitively, larger slits allow more light to pass through, which enhances the SNR. However, to prevent spectral overlaps on the monochrome camera sensor, only a limited number of slits are practical at each horizontal position. Consequently, the spatial resolution is primarily determined by the height of the slits. Additionally, wider slits increase the width of spectral peaks on the monochrome camera, reducing the spectral resolution.

To evaluate the impact of slit size and camera parameters on the SNR, an analysis was conducted using a Hg calibration light source (HG-2 Ocean Insight) with known emission spectral lines. This approach avoids uncertainties arising from the dynamic nature of the experimental reaction scene. The baseline of the signal was removed by fitting the background signal to a linear function using least-squares regression. After baseline removal, the intensity of the emission peak at 696 nm was defined as the signal, while the baseline standard deviation was used to define the noise.

The slit designs used for SNR analysis are shown in Fig. 3. One mask was designed with slits of fixed width at 25 μm, while the other had slits of fixed height at 150 μm. The results of the SNR analysis are presented in Fig. 4, providing insights into the optimal slit dimensions for balancing spatial resolution, spectral resolution, and SNR.

Fig. 4 shows that within a certain range (width < 35 μm, height < 150 μm), increasing the slit width or height improves the SNR, while

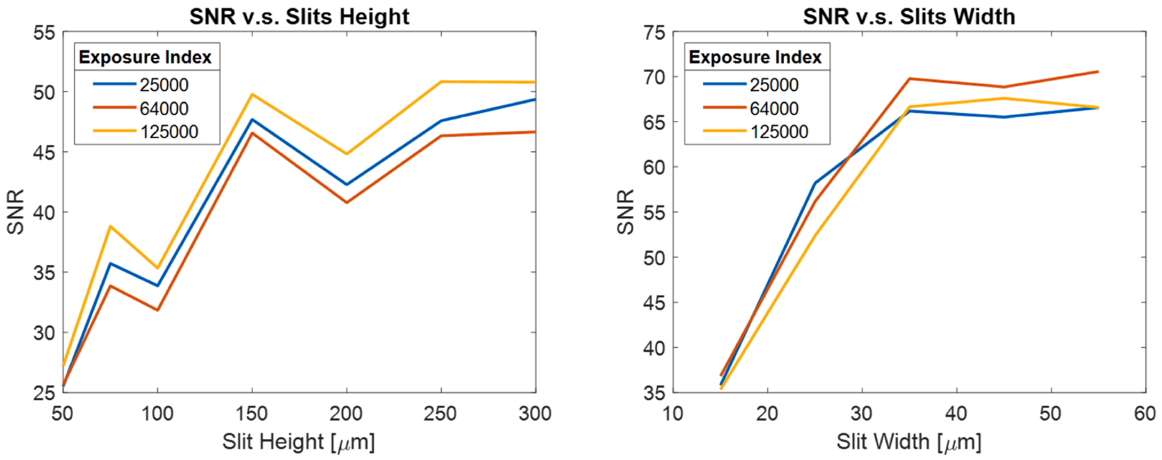

Fig. 4. SNR changes with different slit heights (left) and slit widths (right) at camera exposure index of 25,000, 64,000, 125,000.

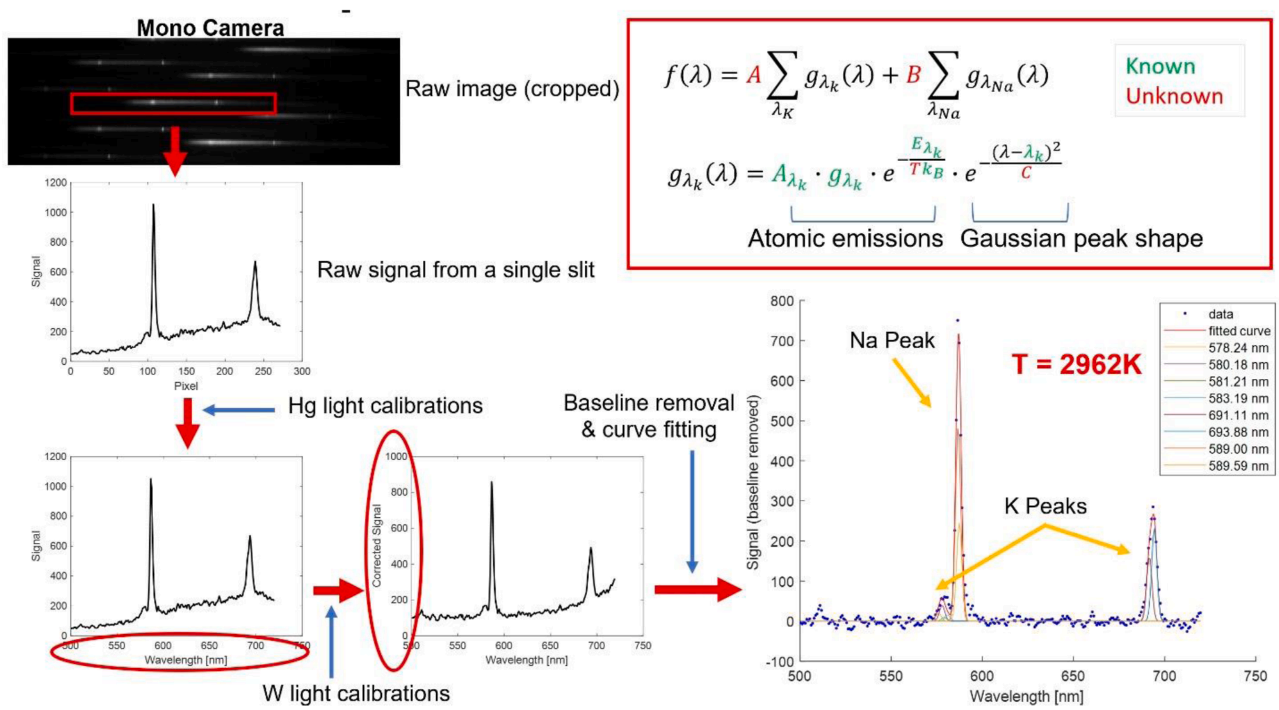

Fig. 5. Data processing overview. The processes of signal extraction, data correction using calibration results, and baseline removal are indicated by the red arrows step-by-step. The equations used for curve fitting are shown in the upper right corner. The peak fitting curve is presented as the red line in the lower right plot, with detailed curves for each emission peak displayed in different colors, as indicated by the legend. An enlarged plot for emission peak with curve fitting is provided in Supplementary Materials (Figure S6).

changes in the camera's exposure index[1] have minimal impact on the SNR. However, as the slit size becomes larger, the improvement in light intensity diminishes. In the vertical direction, since light is dispersed horizontally by the diffraction grating, increasing the slit height only expands the pixel areas capturing the spectral lines, without significantly enhancing the signal. For horizontal direction, increasing the slit width does increase the total light collected for each spectral line, but it also broadens the emission peaks, offsetting the benefit of increased light intensity. For example, the full width half maximum (FWHM) of the peak increases from 2.9 nm to 3.2 nm when slit width increases from 25 μm to 55 μm.

Considering these factors, the subsequent results employ slits with a width of 25 μm and a height of 150 μm, optimizing the balance between SNR, spatial resolution, and spectral resolution. The slits are aligned in a 2D arrangement on the mask, as illustrated by Mask C in Fig. 3. With the current 10× objective lens, this slit size captures the light emitted from a 2.5 μm× 15 μm area. The slits distribution enables a spatial resolution of 250 μm vertically and 200 μm horizontally, as defined by the distance between adjacent slits.

2.4. *Calibration and data processing*

The raw data captured by the monochrome camera represents the electric signal output from each pixel sensor. For spectral analysis, the pixel locations must be correlated with specific wavelengths. In addition, the camera sensor, along with the intensifier and optical system, has varying responses to different wavelengths at different pixel locations. Therefore, calibration is essential to convert the raw signal into light intensity values from the combustion events.

A Hg calibration light source, as mentioned in Section 2.3, was used to determine the pixel-to-wavelength correlation factors for the spectra captured through each slit. The vertical positions of the spectral lines were identified by summing the image matrix horizontally and applying peak identification functions. For each spectral line, 5–6 signal peaks were matched to the known Hg light source peak positions, from which pixel-to-wavelength factors and the horizontal range of the spectral lines are determined. The current setup has a spectral resolution of 1.5 nm/pixel.

To correct the system's wavelength response, a tungsten halogen light source (the same one for pyrometry calibration, as mentioned in Section 2.1.1), was used. Correction factor profiles as function of wavelength were determined by dividing the measured spectral signals by the theoretical radiation profile of the light source.

The data processing pipeline is illustrated in Fig. 5. The spectral line profiles were extracted from the images captured by the monochrome camera using the line boundaries established during the calibration process. Vertical averaging was performed to reduce random noises. A pixel-to-wavelength transformation was then applied using the wavelength calibration data, followed by intensity corrections based on the tungsten light correction factors. The baseline of the corrected signal was removed using second-order polynomial fitting to the logarithm of the baseline data.

As shown in Fig. 5, a strong Na peak at approximately 589 nm partially overlapped with the K emission peak at 580 nm. This contamination is caused by ubiquitous nature of Na impurities. In addition, multiple K emission peaks exist near 580 nm and 694 nm [32], but these peaks cannot be fully resolved due to the current spectral resolution.

To address the interference from Na peaks and account for all K peaks, a custom function fitting approach was developed, as illustrated in Fig. 5. The function is defined as the summation of Na and K peaks, with two multipliers A and B isolating Na and K emissions, respectively. Each peak at wavelength λ_k is defined as the product of the atomic emission equation and a Gaussian peak shape. The parameters A_{λ_k}, g_{λ_k} and E_{λ_k} are properties obtained from the NIST Atomic Spectra Database [32]. The gaussian peak width factor C was constrained to within 5 nm

---

[1] In Phantom cameras, the Exposure Index (EI) adjusts the effective ISO and does not change the exposure time

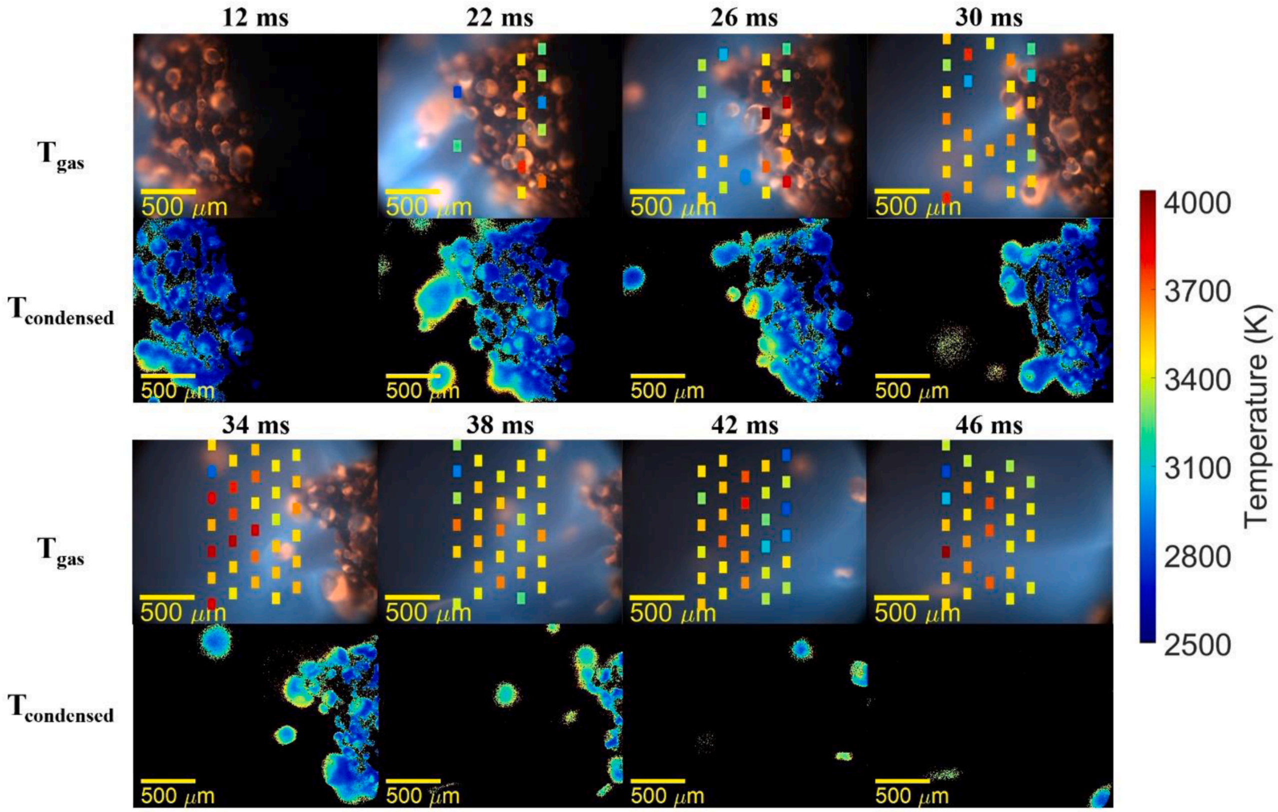

Fig. 6. Evolving Al-$KClO_4$ thermite (φ= 1.75) at different times. Upper: original RGB camera images with gas phase temperature marked at colored slit positions. Lower: Three-color pyrometry images showing the condensed phase temperature distribution. Areas with low light intensities have been filtered out.

to minimize the impact from baseline noise near the signal.

The temperature is extracted directly as a fitting parameter, with uncertainty defined as half the 68 % confidence interval range. This process was iteratively applied to all spectral lines in a single image and repeated across other frames.

2.5. Sample preparation

Prior to each test, 3D-printed Al-$KClO_4$ composites with 90 wt% loading were prepared. Details of the 3D printing method can be found in prior work [33]. Briefly, the 3D-printing ink was prepared by first dissolving the binder materials, 4 wt% polyvinylidene fluoride (PVDF) and 6 wt% hydroxypropyl methylcellulose (HPMC), in 4 mL of dimethylformamide (DMF) under magnetic stirring. Once the binders were fully dissolved, the oxidizer, $KClO_4$, was added and allowed to dissolve completely before introducing aluminum nanoparticles (Al NPs, 80 wt% active content, purchased from US research nanomaterials Inc, 100 nm). The ink was then ultrasonicated for 30 min, followed by overnight magnetic stirring. Prior to loading into the printing syringe, the ink was sonicated again for 30 min to ensure homogeneity. The amounts of $KClO_4$ and Al NPs were calculated based on the equivalence ratio for the reaction of $8Al + 3KClO_4 \rightarrow 4Al_2O_3 + 3KCl$.

During printing, the ink was extruded through a 16-gauge nozzle onto a glass substrate heating to ~75 °C, forming a pre-designed 15-layer pattern. The printed thermite sticks were left on the glass substrate overnight to allow the solvent to fully evaporate. The thermite was then cut into ~ 2 cm sticks for combustion imaging tests. The thermite typically has a wide of 2.0 ± 0.2 mm and a thickness of 1.1 ± 0.1 mm.

For combustion tests, the sample and a NiCr ignition wire (Ted Pella Inc) were mounted on the slot of a right-angle bracket (Thorlabs AB90D). This bracket was placed inside a 9.5 × 9.5 × 9.5 cm acrylic box with customized inlet port and optical window (see Supplementary Materials, Figure S1). The box was not airtight and is assumed to maintain ambient pressure (~1 atm). Once the box was filled with argon, the sample was ignited via joule heating of the NiCr wire using a power supply set to 35 V and 3.0A.

3. Experimental demonstrations with Al-$KClO_4$ thermites

The system was used to capture reaction scenes and measure both gas-phase and condensed-phase temperatures of Al-$KClO_4$ thermites under high frame rate (5000 fps for gas-phase, 10,000 fps for condensed-phase). With these frame rates, the temporal resolution is 0.1 ms for condensed-phase temperatures and 0.2 ms for gas-phase temperatures. Fig. 6 presents the burning process and corresponding spatially resolved gas and condensed phase temperatures for an Al-$KClO_4$ thermite with an equivalence ratio of 1.75. This equivalence ratio was chosen to clearly demonstrate the sintering phenomenon of melting Al, providing a comprehensive showcase of the system's ability to measure temperatures in both solid and gas phase. The top panels in Fig. 6 illustrate the gas-phase temperature results at each slit position, with the slit positions represented as rectangles overlay on the combustion scene captured by the RGB camera. To enhance visibility, the rectangles are enlarged and do not reflect the actual slit sizes. The color of each rectangle corresponds to the gas-phase temperature, as indicated by the color bar on the right side of Fig. 6. Gas-phase temperature data with uncertainties (defined in Section 2.4 as half of the 68 % confidence interval from the spectral fitting) exceeding 350 K were excluded. Despite some variations and outliers due to signal noise and fitting uncertainty, the gas-phase temperatures are generally in the range of 3400–3700 K when the thermite reaction front is in camera scene, where the distance from slits to the reaction front is within ~1.5 mm. These measured values are comparable with thermo-chemical equilibrium calculations of the adiabatic flame temperature carried out with Cheetah [34](Fig. 9).

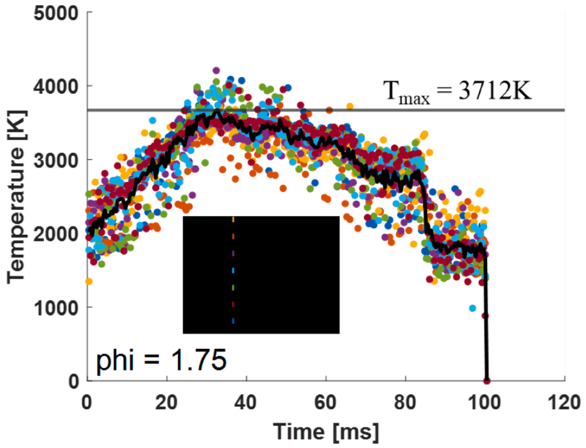

Fig. 7. Gas phase temperature temporal profiles for selected slits. Data points colors correspond to the slit position as indicated by the image at the bottom, with the black rectangle representing RGB camera frame. Averaged temperature curve is shown as the black line, with the maximum value defined as the peak gas phase temperature at this equivalence ratio.

The pyrometry measurements indicate that the temperatures of the melting Al droplets range from 2600–2800 K, and thus close to the boiling temperature of aluminum (2743 K [35]). The burning thermite reveals a multi-step Al reaction process, including melting, sintering, evaporation, and condensation. Observations also show the formation of Al_2O_3 caps on most melting Al droplets, with cap temperatures around 3100 K, which aligns with previous study by Wang et al [36].

A comparison of the gas-phase and condensed-phase temperatures within the same frame shows that the gas-phase temperatures are approximately 600 K higher than the condensed-phase temperatures. This suggest that the most exothermic reactions are occurring in the gas phase, as aluminum is known to burn in the vapor phase [37].

Fig. 7 illustrates the gas-phase temperature profiles as a function of time for a group of selected slits. All slits exhibit similar temperature temporal trend and have peak gas-phase temperatures of approximately 3600–4000 K. The averaged temperature for the selected slit is shown as the black line. Peak gas phase temperature is defined as the maximum value of the averaged temperature curve, and standard deviation is calculated at the time corresponding to the peak temperature. Notably, the peak gas-phase temperature 3712 K is about 1000 K higher than the condensed-phase temperatures, further validating the observation from Fig. 6 that the most exothermic reactions are occurring in the gas phase.

To further explore the complex reaction phenomenon, an analysis was conducted for Al-$KClO_4$ thermites at varying equivalence ratios. Fig. 8 reveals a clear transition in reaction behavior: under fuel-lean conditions, Al is primarily ejected from the reaction front as small particles; under fuel-rich conditions, Al tends to melt, sinter and form larger droplets that roll on the thermite surface before leaving the reaction zone. Under fuel rich conditions, the oxidation of Al is expected to be mainly in the gas evaporating from the melting droplets.

The time-resolved temperature curves at the same slit positions on Fig. 7 for each equivalence ratio are provided in supplementary materials (Figure S7), from which the peak gas-phase temperature and its variation across selected slits are obtained. As shown in Fig. 9, the maximum gas-phase temperatures at different equivalence ratios align well with the theoretical adiabatic temperatures of Al-$KClO_4$ reactions.

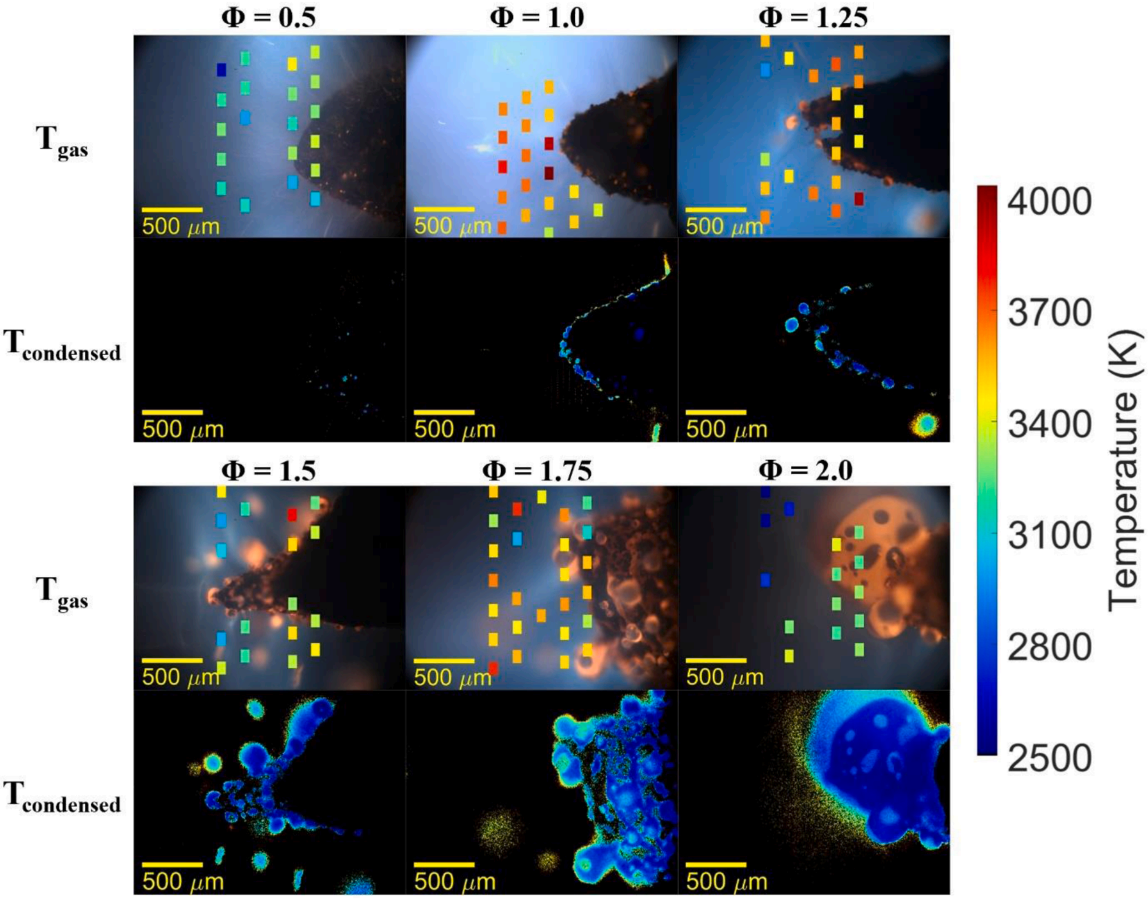

Fig. 8. Al-$KClO_4$ temperature profiles at different equivalence ratios. Upper: original color camera images with gas phase temperature marked at colored slit positions. Lower: Three-color pyrometry images showing the condensed phase temperature distribution. Areas with low light intensities have been filtered out.

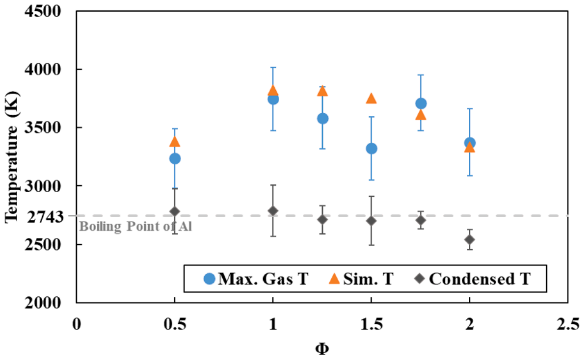

Fig. 9. Al-KClO$_4$ temperatures at various equivalence ratios. Max. Gas T: maximum temperatures of the slits-averaged gas-phase temperature curves, from emission spectral measurement. The error bar represents the averaged standard deviation of temperatures across the selected slits. Sim. T: simulated adiabatic temperatures from Cheetah. Condensed T: condensed-phase temperatures of melting aluminum droplets, from pyrometry measurement. The gray dashed line at 2743 K indicates the boiling temperature of aluminum.

From equivalence ratio 1 to 1.75, the gas-phase temperatures have minimal changes that are within the accuracy of the measurement. At equivalence ratio 0.5 and 2, a slightly lower gas-phase temperature can be observed. The condensed-phase temperatures remain constant with various equivalence ratios, close to the boiling temperature of aluminum.

The observations demonstrate that the equivalence ratio significantly impacts Al reaction behavior and heat transfer mechanisms. At all tested equivalence ratios, the gas-phase temperatures near the reacting front are consistently higher than those of the condensed phase, highlighting the dominant contribution of gas-phase reactions to heat release during combustion. Under fuel-lean conditions, Al is ejected and reacts primarily as small particles, while under fuel-rich conditions, Al tends to sinter on the thermite surface, forming larger droplets. One possible explanation for the observed trends is that, melting and sintering of Al on the reaction surface enhance conductive heat transfer to the unburned region. However, this process may also reduce the available surface area for aluminum evaporation, thereby hindering gas-phase heat release. This could account for the slightly lower gas and condensed phase temperatures observed at an equivalence ratio of 2.

4. Conclusion

This paper describes the development of a high-speed imaging system capable of hyperspectral imaging and pyrometry imaging for transient reaction scenes, enabling simultaneous spatially and temporally resolved vapor- and condensed phase temperature measurement during combustion. The system design and data processing methods are described in detail, including optimization of the slit shape of the mask, implementation of a brute-force minimization method for pyrometry, and extraction of gas-phase temperatures through spectral signal fitting.

The system was demonstrated using 3D-printed Al-KClO$_4$ thermites, showing the temporal temperature measurements for reactions at an equivalence ratio of 1.75, and comparing gas- and condensed-phase temperatures across equivalence ratios from 0.5 to 2. These findings reveal the complex interplay between thermal and chemical processes in governing the reaction dynamics of energetic composites. A hypothesis is proposed that the thermite reaction is governed by a trade-off between enhanced conductive heat transfer from molten Al on the reaction surface and reduced Al evaporation due to sintering, which further limits the gas-phase reactions.

This study presents a valuable diagnostic tool for studying heterogeneous combustion processes with high temporal and spectral resolution, providing insights into heat release mechanisms and multi-phase interactions for Al-KClO$_4$ reactions. Although the current system has limited spatial resolution for its spectral imaging arm, it has the potential to be upgraded to a higher-resolution hyperspectral configuration, with trade-offs in wavelength range and spectral resolution. This approach is adaptable to other high-temperature reactive systems and lays the foundation for advanced imaging in energetic material research.

CRediT authorship contribution statement

Qinghui Meng: Writing – original draft, Visualization, Methodology, Formal analysis, Data curation. **Erik Hagen:** Visualization, Formal analysis. **Colin Goodman:** Writing – review & editing, Formal analysis. **Mark A. Foster:** Writing – review & editing, Methodology, Investigation, Conceptualization. **Michael R. Zachariah:** Writing – review & editing, Project administration, Methodology, Investigation, Funding acquisition, Conceptualization.

Declaration of competing interest

On behalf of all the authors, we declare no conflict of interest. This work is original and has not been considered for publication elsewhere.

Acknowledgements

This research was funded by the DTRA-MSEE URA and the ARO. A Navy DURIP grant was used for acquisition of components.

Supplementary materials

Supplementary material associated with this article can be found, in the online version, at doi:10.1016/j.jqsrt.2025.109598.

Data availability

Data will be made available on request.

References

[1] Zhou X, Torabi M, Lu J, Shen R, Zhang K. Nanostructured energetic composites: synthesis, ignition/combustion modeling, and applications. ACS Appl Mater Interfaces 2014;6:3058–74. https://doi.org/10.1021/am4058138.

[2] Badgujar DM, Talawar MB, Asthana SN, Mahulikar PP. Advances in science and technology of modern energetic materials: an overview. J Hazard Mater 2008;151:289–305. https://doi.org/10.1016/j.jhazmat.2007.10.039.

[3] Rossi C, Estève D. Micropyrotechnics, a new technology for making energetic microsystems: review and prospective. Sens Actuators Phys 2005;120:297–310.

[4] Muravyev NV, Monogarov KA, Schaller U, Fomenkov IV, Pivkina AN. Progress in additive manufacturing of energetic materials: creating the reactive microstructures with high potential of applications. Propellants Explos Pyrotech 2019;44:941–69.

[5] Chen N, He C, Pang S. Additive manufacturing of energetic materials: tailoring energetic performance via printing. J Mater Sci Technol 2022;127:29–47. https://doi.org/10.1016/j.jmst.2022.02.047.

[6] Wang H, Kline DJ, Rehwoldt M, Wu T, Zhao W, Wang X, et al. Architecture can significantly alter the energy release rate from nanocomposite energetics. ACS Appl Polym Mater 2019;1:982–9. https://doi.org/10.1021/acsapm.9b00016.

[7] Zeng C, Wang J, He G, Huang C, Yang Z, Liu S, et al. Enhanced water resistance and energy performance of core–shell aluminum nanoparticles via in situ grafting of energetic glycidyl azide polymer. J Mater Sci 2018;53:12091–102. https://doi.org/10.1007/s10853-018-2503-1.

[8] Mondal J, Singh SK, Shin WG. Enhanced ignition and combustion performance of boron-based energetic materials through surface modification and titanium dioxides coating. Ceram Int 2024;50:16598–614.

[9] Wang H, Jacob RJ, DeLisio JB, Zachariah MR. Assembly and encapsulation of aluminum NP's within AP/NC matrix and their reactive properties. Combust Flame 2017;180:175–83. https://doi.org/10.1016/j.combustflame.2017.02.036.

[10] Pang WQ, Yetter RA, DeLuca LT, Zarko V, Gany A, Zhang XH. Boron-based composite energetic materials (B-CEMs): preparation, combustion and applications. Prog Energy Combust Sci 2022;93:101038.

[11] Bolshov MA, YuA Kuritsyn, YuV Romanovskii. Tunable diode laser spectroscopy as a technique for combustion diagnostics. Spectrochim Acta Part B At Spectrosc 2015;106:45–66. https://doi.org/10.1016/j.sab.2015.01.010.

[12] Ramirez RS, Radhakrishna V, Tancin RJ, Schwartz CJ, Ornek M, Son S, et al. Ultrafast-Laser-Absorption-Spectroscopy diagnostics for aluminum and lithium vapor in composite-propellant flames. AIAA SCITECH 2024 Forum; 2024. p. 2421.

[13] Tas G, Franken J, Hambir SA, Hare DE, Dlott DD. Ultrafast Raman spectroscopy of shock fronts in molecular solids. Phys Rev Lett 1997;78:4585.

[14] Richardson DR, Kearney SP, Guildenbecher DR. Post-detonation fireball thermometry via femtosecond-picosecond coherent anti-stokes Raman scattering (CARS). Proc Combust Inst 2021;38:1657–64.

[15] Wang H, Kline DJ, Zachariah MR. In-operando high-speed microscopy and thermometry of reaction propagation and sintering in a nanocomposite. Nat Commun 2019;10:3032. https://doi.org/10.1038/s41467-019-10843-4.

[16] Chen MW, You S, Suslick KS, Dlott DD. Hot spots in energetic materials generated by infrared and ultrasound, detected by thermal imaging microscopy. Rev Sci Instrum 2014;85.

[17] Chen Y, Guildenbecher DR, Hoffmeister KN, Cooper MA, Stauffacher HL, Oliver MS, et al. Study of aluminum particle combustion in solid propellant plumes using digital in-line holography and imaging pyrometry. Combust Flame 2017;182: 225–37.

[18] Demko AR, Hill KJ, Ismael EK, Kastengren A. Observation of aluminum interaction with the binder melt layer using high-speed synchrotron-based phase contrast imaging. Combust Flame 2022;241:112054. https://doi.org/10.1016/j.combustflame.2022.112054.

[19] Skaggs M, Hargather M, Cooper M. Characterizing pyrotechnic igniter output with high-speed schlieren imaging. Shock Waves 2017;27:15–25.

[20] Alemohammad M, Wainwright ER, Stroud JR, Weihs TP, Foster MA. Kilohertz frame rate snapshot hyperspectral imaging of metal reactive materials. Appl Opt 2020;59:10406. https://doi.org/10.1364/AO.402305.

[21] Zhang W, Song H, He X, Huang L, Zhang X, Zheng J, et al. Deeply learned broadband encoding stochastic hyperspectral imaging. Light Sci Appl 2021;10:108. https://doi.org/10.1038/s41377-021-00545-2.

[22] Dwight JG, Tkaczyk TS. Lenslet array tunable snapshot imaging spectrometer (LATIS) for hyperspectral fluorescence microscopy. Biomed Opt Express 2017;8: 1950. https://doi.org/10.1364/BOE.8.001950.

[23] Araújo A. Multi-spectral pyrometry—A review. Meas Sci Technol 2017;28:082002.

[24] Jacob RJ, Kline DJ, Zachariah MR. High speed 2-dimensional temperature measurements of nanothermite composites: probing thermal vs. Gas generation effects. J Appl Phys 2018;123.

[25] Dreizin EL. Experimental study of stages in aluminium particle combustion in air. Combust Flame 1996;105:541–56.

[26] Densmore JM, Biss MM, McNesby KL, Homan BE. High-speed digital color imaging pyrometry. Appl Opt 2011;50:2659–65.

[27] Jaramillo NR, Ritchie CA, Pantoya ML, Altman I. Establishing calibration-free pyrometry in reactive systems and demonstrating its advanced capabilities. Appl Energy Combust Sci 2023;16:100230. https://doi.org/10.1016/j.jaecs.2023.100230.

[28] Lynch P, Krier H, Glumac N. Emissivity of aluminum-oxide particle clouds: application to pyrometry of explosive fireballs. J Thermophys Heat Transf 2010;24: 301–8.

[29] Kalman J, Allen D, Glumac N, Krier H. Optical depth effects on aluminum oxide spectral emissivity. J Thermophys Heat Transf 2015;29:74–82.

[30] Rains TC. Flame emission and atomic absorption spectrometry. M. Dekker; 1969.

[31] Gibson JH, Grossman WE, Cooke W. Excitation processes in flame spectrometry. Anal Chem 1963;35:266–77.

[32] Kramida A., Ralchenko Y., Reader J. NIST Atomic Spectra Database (version 5.5.1), [Online]. Available: https://physics.nist.gov/asd 2017.

[33] Wang H, Shen J, Kline DJ, Eckman N, Agrawal NR, Wu T, et al. Direct writing of a 90 wt% particle loading nanothermite. Adv Mater 2019;31:1806575.

[34] Fried LE. CHEETAH: a fast thermochemical code for detonation. Livermore, CA (United States): Lawrence Livermore National Lab. (LLNL); 1993. https://doi.org/10.2172/10154126.

[35] Zhang Y, Evans JR, Yang S. Corrected values for boiling points and enthalpies of vaporization of elements in handbooks. J Chem Eng Data 2011;56:328–37.

[36] Wang Y, Hagen E, Biswas P, Wang H, Zachariah MR. Imaging the combustion characteristics of Al, B, and Ti composites. Combust Flame 2023;252:112747. https://doi.org/10.1016/j.combustflame.2023.112747.

[37] Glassman I. Combustion. Academic press; 1997.